Journal of Power Sources 196 (2011) 9238–9245

Contents lists available at ScienceDirect

Journal of Power Sources

journal homepage: www.elsevier.com/locate/jpowsour

Sintering and conductivity of $BaCe_{0.9}Y_{0.1}O_{2.95}$ synthesized by the sol–gel method

Agnès Princivalle[a,*], Guilhem Martin[a], Céline Viazzi[a], Christian Guizard[a], Nicolas Grunbaum[b], Laurent Dessemond[b]

[a] LSFC UMR 3080 Saint-Gobain/CNRS 550 avenue Alphonse Jauffret, BP 224, F-84306 Cavaillon Cedex, France
[b] LEPMI, PHELMA Campus, Domaine Universitaire, 1130 rue de la Piscine, BP 75, F-38402 Saint Martin D'Heres Cedex, France

ARTICLE INFO

Article history:
Received 11 March 2011
Received in revised form 11 July 2011
Accepted 13 July 2011
Available online 23 July 2011

Keywords:
Y-doped $BaCeO_3$
Proton conductor
Sol–gel
Impedance spectroscopy

ABSTRACT

Ceramic powders of $BaCe_{0.9}Y_{0.1}O_{2.95}$ (BCY10) have been prepared by the sol–gel method. Barium and yttrium acetate and cerium nitrate were used as ceramic precursors in a water solution. The reaction process studied by DTA–TG and XRD showed that calcination of the precursor powder at $T \geq 1000\,^{\circ}C$ produces a single perovskite phase. The densification behaviour of green compacts studied by constant heating rate dilatometry revealed that the shrinkage rate was maximal at 1430 °C. Sintered densities higher than 95% of the theoretical one were thus obtained below 1500 °C. The bulk and additional blocking effects were characterized by impedance spectroscopy in wet atmosphere between 150 and 600 °C. A proton conduction behaviour was clearly identified. The blocking effect can be related to a space-charge depletion layer of protons in the vicinity of grain boundaries.

1. Introduction

Proton conducting materials, discovered by Iwahara in the early 1980s [1,2] are potentially useful for many electrochemical devices such as fuel cells, hydrogen sensors and steam electrolysers [3–8]. Consequently, $BaCeO_3$-based ceramics have received considerable attention since they exhibit the highest proton conductivity in the family of ABO_3 perovskite-type oxides [3,8,9]. The incorporation of trivalent dopants into the $BaCeO_3$ structure results in the creation of oxygen vacancies. In wet atmospheres, these defects constitute the sites for the incorporation of water. Regardless the mechanism of protons migration in perovskite oxides, oxygen vacancies are the main defects at high temperatures and the dissolution of protons is favoured by decreasing temperature. Thus, proton conductivity is likely to be predominant at low temperatures and oxide ion conductivity is the main contribution at high temperatures [10].

Barium cerates powders are usually fabricated by the conventional solid-state reaction between barium carbonate and cerium oxide. The main drawback of this method is that it is difficult to obtain a homogeneous composition and density green bodies because of the inhomogeneity in shape and size of the initial powders. This yields prolonged calcinations at high temperatures ($T > 1000\,^{\circ}C$) and sintering around 1500 °C [11–15]. During the powder preparation and the milling process, impurity contamination of the sintered bodies can degrade the electrical properties [13,16]. Moreover, these properties depend also directly on the sinterability of these ceramics. Since the microstructure strongly influence the total conductivity of $BaCeO_3$ based ceramics [17–19], it must be monitored to optimize the electrical properties. The goal of this study was the synthesis of very fine yttrium-doped barium cerate powders by a new chemical route and the fabrication of dense and single phase ceramics of controlled composition and microstructure. The conductivity behaviour of the considered samples was investigated by impedance spectroscopy and was compared to that of dense BCY10 prepared from solid-state reaction. In addition, the origin of the recorded blocking effect in these polycrystalline ceramics is discussed.

2. Experimental Procedure

2.1. Preparation of $BaCe_{0.9}Y_{0.1}O_{2.95}$ sintered pellets

For sol–gel method, the starting materials were barium acetate $Ba(CH_3COO)_2$ (99–102%, Alfa Aesar), nitrate cerium $Ce(NO_3)_3{\cdot}6H_2O$ (99.99%, Alfa Aesar) and yttrium acetate $Y(CH_3COO)_2{\cdot}4H_2O$ (99.9%, Alfa Aesar). The precursors were weighed to yield the composition $BaCe_{0.9}Y_{0.1}O_{2.95}$ and dissolved in distilled water. An organic solution with a mixture (10:90 wt.%) of ethylene glycol (Fluka) and isopropanol (Acros Organics) was added so that the organic solution represents 50 wt.% of the final solution. It was stirred at 90 °C until it turned into a white gel which was annealed at 600 °C for 2 h. The powders were ground in a mortar. The as-obtained powders were calcined in air at 1100 °C for 8 h, subsequently ball milled in isopropanol for 24 h and then sieved. The dried pow-

* Corresponding author. Tel.: +33 4 32 50 03 03; fax: +33 4 32 50 09 04.
E-mail address: agnes.princivalle@saint-gobain.com (A. Princivalle).

0378-7753/$ – see front matter © 2011 Elsevier B.V. All rights reserved.
doi:10.1016/j.jpowsour.2011.07.048

ders were examined by X-ray powder diffraction analysis (X'pert PANALYTICAL). Simultaneous thermogravimetric analysis and differential thermal analysis (TGA/DTA, NETZCH) were carried out in air. Samples were heated from 25 up to 1400 °C at a heating rate of 10 °C min^{-1}. Powder morphology was characterized by scanning electron microscopy (SEM) (JEOL 6301F), and BET (QUANTACHROM, Nova 2000). The ball milled calcined powders, without adding binders, were uniaxially cold pressed into pellets (12 mm in diameter and about 3 mm in thickness) at 200 MPa. The green density was about 60% of theoretical density (6.21 g cm^{-3}). For solid-state reaction, barium carbonate $BaCO_3$ (99%, Aldrich), cerium oxide CeO_2 (99.99%, Alfa Aesar) and yttrium oxide Y_2O_3 (99.9%, Acros Organics) were used as starting materials. Proper amounts were ball milled in ethanol (Acros Organics) for 24 h. After drying, the powder was calcined at 1100 °C for 8 h, ball milled in ethanol for 24 h and sieved. The as obtained powder was uniaxially cold pressed at 200 MPa and sintered at 1600 °C for 6 h in air (heating rate: 100 °C h^{-1}).

The sinterability of green compacts from sol–gel route was investigated by dilatometry (SETARAM SETSYS Evolution 1750). A constant heating rate of 10 °C min^{-1} was adopted. The green pellets were sintered in air from 1230 °C to 1630 °C for 6 h in air (heating rate: 100 °C h^{-1}). In order to avoid any reaction between samples and the crucible (alumina or zirconia), a thick layer of the calcined powders with the same composition was put between the pellet and the crucible [13,20]. Bulk density and open porosity were measured by the imbibition method using water as the liquid medium. Sintered pellets were characterized by X-ray diffraction (XRD). The microstructure of sintered pellets was examined by SEM. The average grain size, d_g, was measured from SEM pictures using a line-intercept method taking into account at least 300 grains.

2.2. Electrical measurements

In order to avoid any interference between the proper blocking effect of grain boundaries and that of porosity, impedance measurements were only performed on dense pellets (>95% of the theoretical density), i.e. samples synthesized by sol–gel (SG) and sintered at 1500, 1550 and 1600 °C and pellet prepared from solid-state (SS) reaction and sintered at 1600 °C. The corresponding samples will be thus referenced as SG1500, SG1550, SG1600 and SS1600. On each face of the ceramic pellets, platinum was sputtered at room temperature (EMITECH SC7620 Sputter coater). Accordingly, no thermal firing was required and the adhesion of measuring electrodes was checked before and after electrical measurements. The thickness of platinum was of the order of 100 nm and a sufficient percolation of the film was achieved resulting in a sheet resistance as low as 1 Ω at room temperature. Hence, no significant series resistance due to measuring electrodes was evidenced in the chosen experimental conditions. Platinum meshes were used as current collectors. Impedance spectroscopy measurements were performed on symmetrical cells between 150 and 600 °C in wet (3% H_2O or D_2O) argon flow (0.1 L min^{-1}). A constant atmosphere was maintained by introducing the gas mixture passed through a gas diffuser in water at room temperature. The water vapour pressure was found equal to 3×10^3 Pa. Impedance diagrams were recorded under zero dc conditions (HEWLETT PACKARD 4192ALF) between 5 and 1.3×10^7 Hz. The numbers on impedance diagrams indicate the logarithm of the measuring frequency. Impedance diagrams have been normalized by the geometrical factors of the pellets.

3. Results and discussion

3.1. Powders synthesis and morphology

The thermal evolution of XRD patterns for $BaCe_{0.9}Y_{0.1}O_{2.95}$ precursor obtained by sol–gel and calcined between 600 and 1200 °C

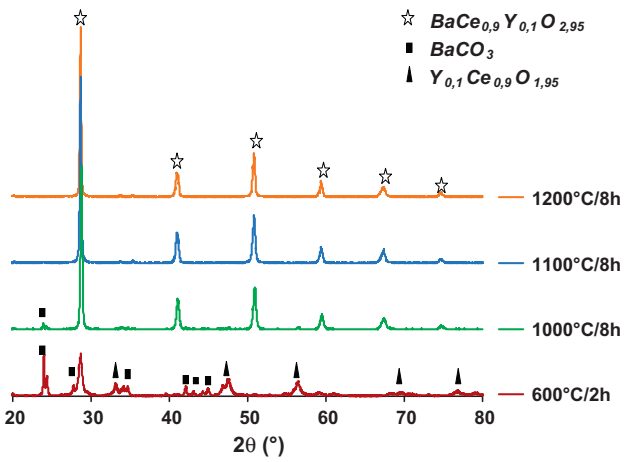

Fig. 1. X-ray diffraction patterns recorded after different thermal treatments.

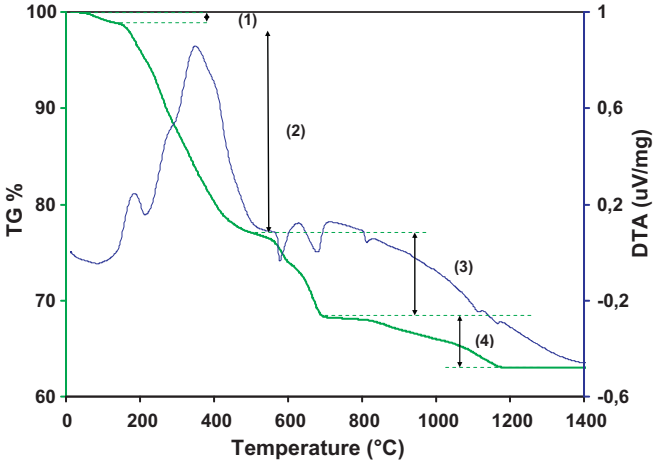

Fig. 2. DTA–TG curves for the BCY10 gel.

are presented in Fig. 1. Heating at 600 °C for 2 h in air results in the formation of $BaCeO_3$, CeO_2 and an yttrium–cerium oxide. These phases can be regarded as resulting from the oxidation of metallic ions. The TGA curves in air of the dried precursor gel present several weight loss steps (Fig. 2). A first steady weight loss occurs from room temperature up to 170 °C. This is usually associated with the elimination of residual water or the release of organic additives from the surfaces of powders [13,21]. A sharp fall in the specimen weight is observed between 170 and 500 °C related to the combustion of polyethylene glycol, which is an exothermic process in the DTA curve [22]. The weight loss up to 700 °C corresponds to the formation of barium carbonate and an yttrium–cerium phase, in agreement with XRD analysis (Fig. 1). The last weight loss, beginning around 800 °C, is ascribed to the thermal decomposition of barium carbonate [23]. This is confirmed by XRD analysis since a few traces of $BaCeO_3$ can be detected after calcination at 1000 °C. No weight change occurs above 1150 °C, indicating that the single phase perovskite is already formed.

XRD results show that the decomposition of carbonates and the perovskite formation complete at 1100 °C, but the TGA curve revealed that these reactions finish at around 1200 °C. This is due to the difference in the time spent at the measuring temperature: the powders investigated by XRD were maintained at the calcination temperature for 8 h, whereas the gel studied by TGA was only briefly exposed at the corresponding temperature.

If one refers to the results of Fig. 1, one can expect a calcination of the precursor gel at 1200 °C. Nevertheless, this will result in a

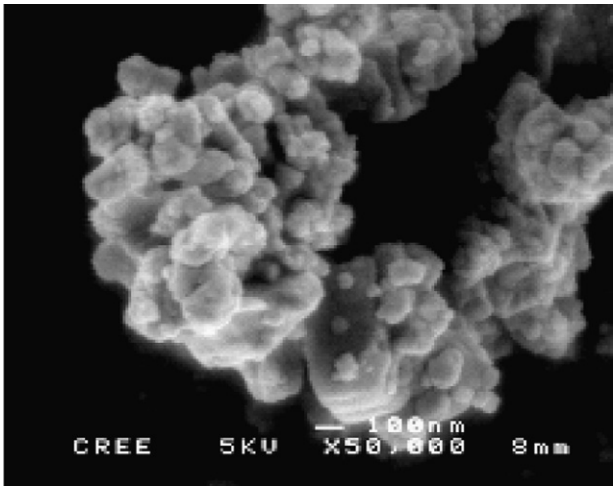

Fig. 3. SEM image of polycrystalline BCY10 powder calcined at 1100 °C for 8 h in air.

decrease of the specific surface area [24] and the powders can react with crucibles at this temperature [13,20]. Accordingly, calcination at 1100 °C was chosen in this study. It should be noted that the synthesis temperature of the sol–gel precursor is lower compared to the conventional solid-state reaction method [12] and is of the order of those reported for other precursor routes [21,25].

The morphology of ball-milled BCY10 powders calcined at 1100 °C is shown in Fig. 3. It consists of small agglomerates composed of small particles in the submicrometer range (20 nm, 500 nm) with an average diameter about 0.2 μm. The measured specific area is equal to 7.8 $m^2 g^{-1}$, which is relatively higher than some literature data [13,24]. Such morphology allows obtaining higher green densities and improving densification, as discussed below.

3.2. Sintering behaviour

The shrinkage curves of a pressed compact are shown in Fig. 4. The sol–gel sample exhibits a large shrinkage since it reaches a value of 20% up to 1600 °C. The shrinkage rate is maximum at around 1430 °C. By determining the density as a function of dwell time at 1400 °C (not shown here), it appears that sintering at least for 6 h in air is required to reach sufficient high relative densities. Thus, all the sintering procedures were performed for 6 h. The absence of any inflexion point on the shrinkage curves above 1400 °C suggests that no significant barium loss occurred up to 1700 °C in air, in agreement with XRD patterns recorded on sintered pellets (Fig. 5). Regardless of the heating temperature, only the perovskite phase was detected. Fig. 6 shows the sintered density as a function of the sintering temperature. No significant sintering occurred below 1200 °C. The comparison with the results reported by Zhong [20] indicates that the sinterability of the as obtained powders is higher, mainly because of a small particle size. It can be seen that when the sintering temperature exceeded 1400 °C, densities higher than 95% of the theoretical one, as well as no open porosity, are obtained. This confirmed by SEM analysis (Fig. 7). Only one kind of morphology was observed for dense samples. The microstructural features of the corresponding ceramics are summarized in Table 1. The average grain size increases with the sintering temperature, as expected. No secondary phases were detected. In the absence of any precipitation of alumina or zirconia at grain boundaries, one can conclude that ball milling did not introduce impurities and that using a BCY10 buffer prevents from any contamination from the crucible.

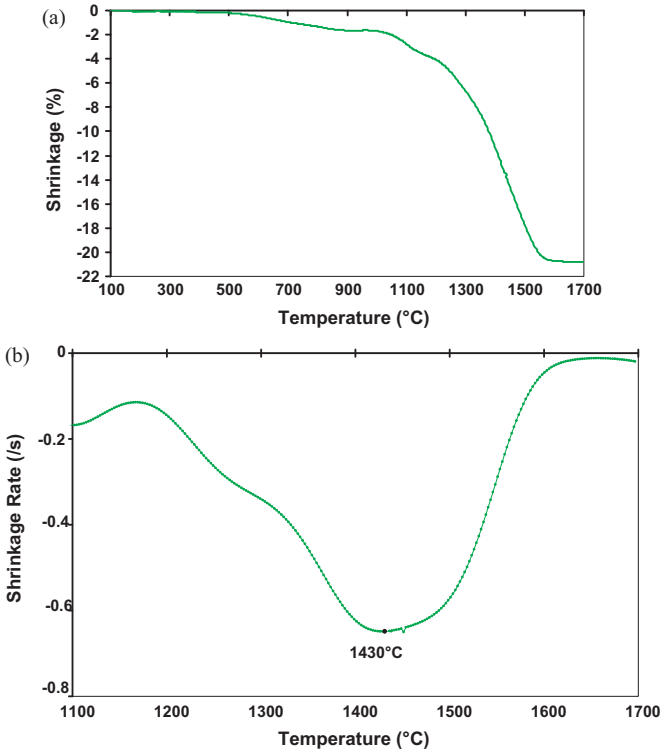

Fig. 4. (a) Shrinkage curve of BCY10 prepared by sol–gel method. (b) Shrinkage rate versus heating temperature.

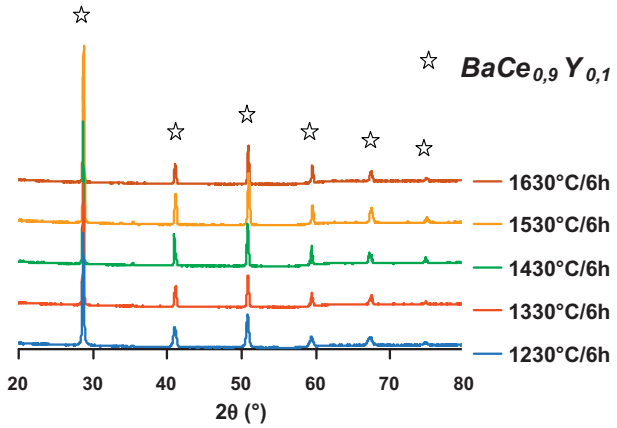

Fig. 5. X-ray diffraction patterns recorded on BCY10 sintered pellets (sol–gel method).

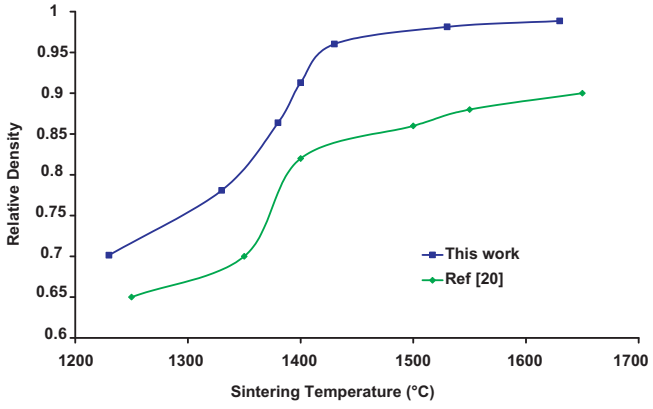

Fig. 6. Comparison with literature data of the relative density versus sintering temperature for BCY10 sol–gel derived material.

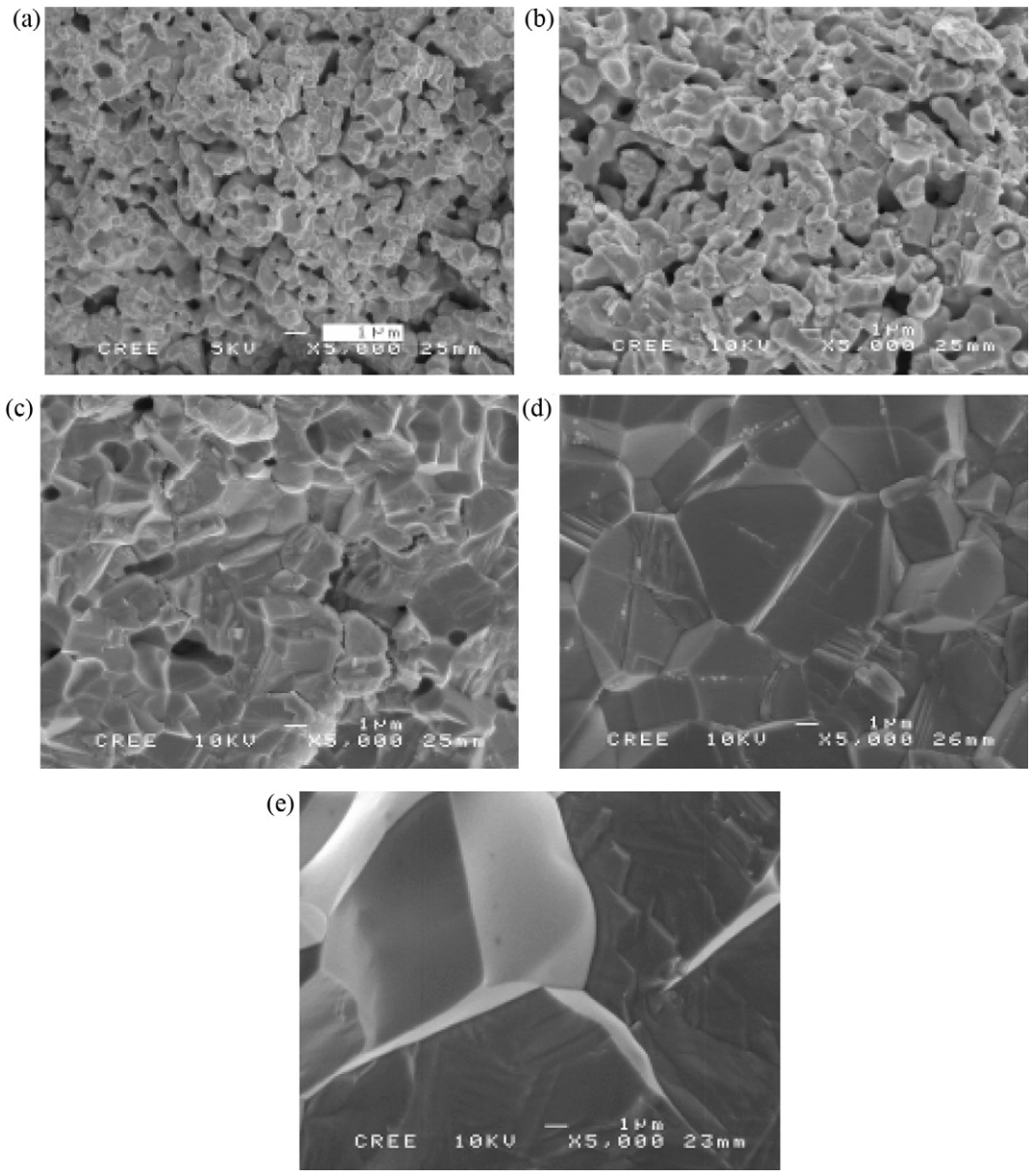

Fig. 7. SEM images of pellet fractures of BCY10 (sol–gel method) sintered at (a) 1230 °C, (b) 1330 °C, (c) 1430 °C, (d) 1530 °C and (e) 1630 °C for 6 h in air.

3.3. Conductivity measurements

In dense and pure polycrystalline ionic conductors, the impedance diagram is typically composed of a high frequency semi-circle, referred to as b, which describes the electrical properties of the grains of the material (bulk) and an intermediate frequency additional contribution, referred to as bl, which represents the blocking effect of charge carriers at grain boundaries [26]. The tail evidenced in the low frequency range, referred to as ele, is related to processes occurring at the interface between platinum electrodes and gas. Impedance spectroscopy was used to probe the relative contributions of bulk and blocking effect to the total conductivity of BCY10 pellets. This technique is as also a powerful tool to correlate electrical properties and microstructure features determined by SEM. Impedance diagrams recorded at around 200 °C in wet argon are shown in Fig. 8. The corresponding results are compared with those determined on a dense pellet prepared by solid-state reaction to put in prominence the effect of the processing route of powders. For the latter sample, the relative density was 98% of the theoretical one and the mean grain size was found equal to 6.2 μm.

For temperatures below 250 °C, three well separated contributions are observed, thus confirming that porosity is low. The observed separation of the electrolyte impedance from the electrode characteristics indicates that the platinum electrodes perfectly match the outer surface of the pellets. Moreover, this ensures that no additional microstructure defect response, apart from the grain boundaries blocking effect, is described. In this study, the experimental diagrams were fitted, using the ZView® software

Table 1
Microstructural features of dense BCY10 pellets.

Sintered BCY10 pellets	Relative density	Closed porosity (%)	Grain size d_g (μm)
SG1500	0.977	1.020	5.5
SG1550	0.970	1.328	6.3
SG1600	0.978	0.735	8.9
SS1600	0.981	1.151	6.2

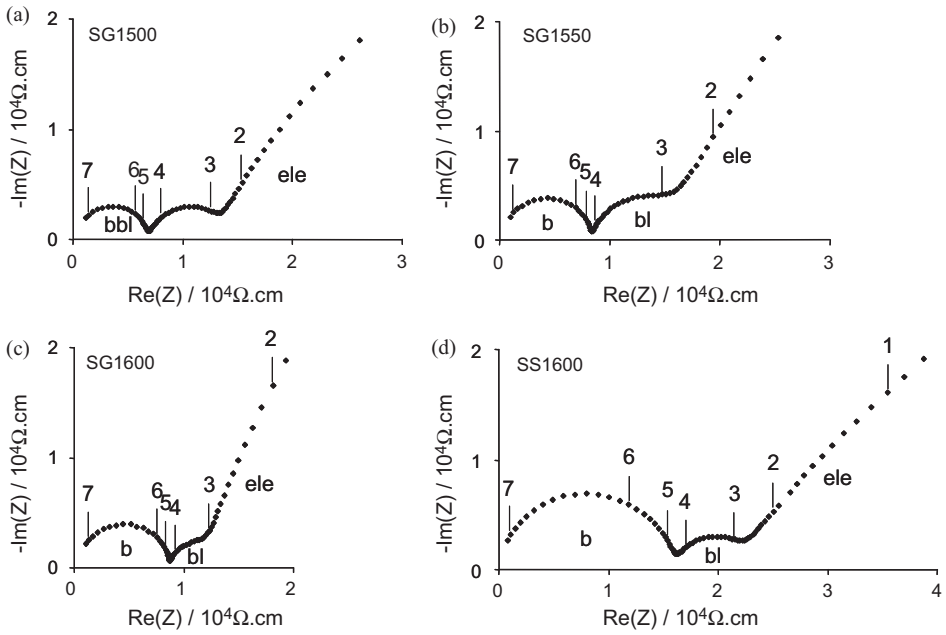

Fig. 8. Impedance diagrams recorded at 200 °C in Ar + 3% H_2O on dense BCY10 from sol–gel route and solid-state reaction. The numbers indicate the logarithm of the measuring frequency.

(Scribner Associates), according to the equivalent circuit shown in Fig. 9 where the resistances $R1$ and $R2$ correspond respectively to the bulk and blocking effect features. The electrode characteristics were described by one or two elementary contributions (resistances $R3$ and $R4$) depending on the measuring temperature. The origin of these latter contributions was not detailed since it is outside the scope of this study. The constant phase element, CPE, added replace pure capacitances to appropriately describe the non-ideal behaviour of semicircles depressed below the real axis in the Nyquist plane. The impedance of a CPE element is given by $Z(\omega) = [Q(i\omega)^n]^{-1}$, where Q and n are fitting parameters and ω is the angular frequency of the measuring ac signal. The value of the capacitance (C) was calculated according to $C = [R^{1-n}Q]^{1/n}$, where R is the span of the semicircle. Another peculiar parameter which can be extracted from impedance data is the apex frequency (f) of a contribution (determined at the minimum of the imaginary part of the recorded contribution in the Nyquist plane) according to $f = [2\pi RC]^{-1}$, which represents an identification signature of a described phenomenon. By increasing temperature, a high frequency inductive effect, originating from the platinum wires in the measurement rig was evidenced and then taken into account by adding an inductive component (L) in series in the corresponding equivalent circuit (Fig. 9). Thus, only the total resistance R_t of the material, which represents the sum of resistances $R1$ and $R2$ (bulk + blocking effect), was determined accurately above 350 °C.

The capacitance values for the high and low frequency semicircles related to the ceramic impedance, described above typically 5×10^2 Hz in the conditions of Fig. 8, were found to be about 4.5–6 pF cm^{-1} and 5–10 nF cm^{-1} (Fig. 10), in agreement with previous reports on doped barium cerate ceramics [15,17,21]. These capacitances are independent of temperature up to 350 °C. As shown in Fig. 8, the frequency distribution of the overall ceramic impedance does not depend on both grain size and elaboration route, in agreement with literature results [27,28]. Moreover, each apex frequency is similar for all investigated samples (Fig. 10), indicating a common origin for each individual impedance contribution to the electrolyte impedance. The high frequency semicircle (b) can be unambiguously assigned to the bulk response and that described in the intermediate frequency range (bl) to the blocking effect of charge carriers at grain boundaries in the studied samples.

Fig. 11 shows the Arrhenius diagrams of bulk (σ_b), blocking (σ_{bl}), specific (σ^s_{bl}) and total (σ_t) conductivities for dense BCY10 in wet argon. Regardless the sintering temperature, the total conductivity of samples prepared by sol–gel route is always higher. For example, σ_t is around 5×10^{-3} S cm^{-1} at 500 °C for sol–gel samples and is equal to 3×10^{-3} S cm^{-1} by using solid-state reaction. It is worth mentioning that the former values obtained for coarse grained ($d_g \geq 5$ μm) are comparable with the state-of-art cerate materials [29,30]. A peculiar feature on the Arrhenius diagram of σ_t is a slope change around 350 °C which is visible for all samples. Such a change has been already detected for yttrium-doped barium cerates either for the bulk conductivity [15] or the total conductivity [21,27,28]. Without emphasizing on the origin of this bending, it is not likely to be due to dehydration of protons [31]. Accordingly, the activation energy of σ_t could not be determined accurately within the whole temperature range and was only calculated for temperatures below 350 °C. The corresponding values are reported in Table 2. They are of the order (0.5 eV) of those which can be attributed to protons as charge carriers [32,33]. The total conductivity measured under water atmosphere (Ar–H_2O) was found higher than under heavy water (Ar–D_2O), in agreement with literature data [34,35]. Below 600 °C, the ratio of both conductivities was found equal to 1.30–1.40, which is close to the theoretical value of $\sqrt{2}$ [36,37]. This isotope effect indicates that BCY10 has a pro-

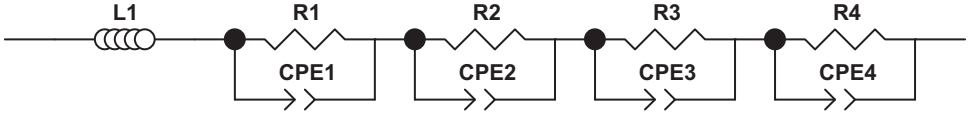

Fig. 9. Equivalent circuit used for impedance diagrams fitting.

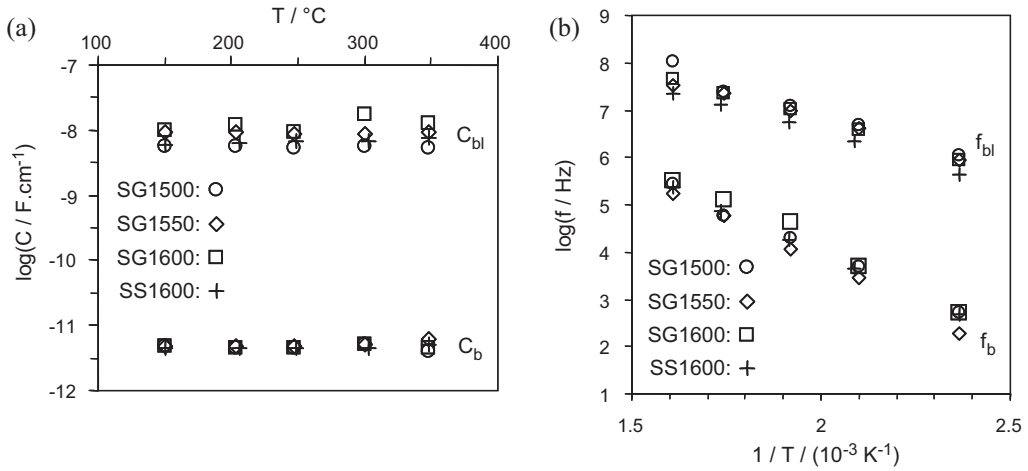

Fig. 10. (a) Bulk and blocking capacitances versus temperature. (b) Arrhenius diagrams of apex frequencies for bulk and blocking impedances (Ar + 3% H_2O).

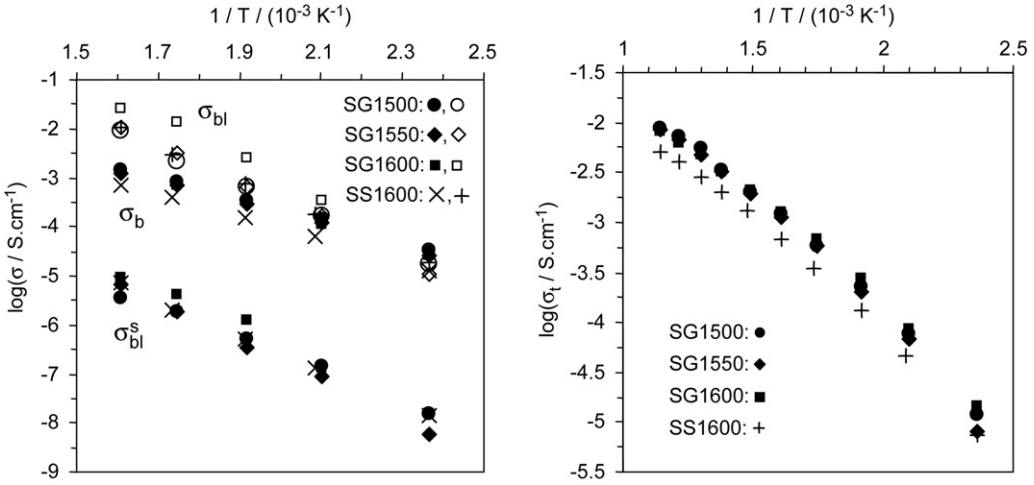

Fig. 11. Arrhenius diagrams of (a) bulk, blocking and specific blocking conductivities and (b) total conductivity (Ar + 3% H_2O).

ton conduction in the chosen experimental conditions. Another argument in favour of this interpretation is that the total conductivity does not change significantly as a function of the water partial pressure for temperatures below 650 °C [38]. Accordingly, the recorded thermal activation is likely to mainly originate from the proton conduction mechanism. The activation energy of the bulk conductivity remains nearly unchanged versus the sintering temperature and the elaboration route (Table 2) and agrees with literature values for ionic conduction in cerate based perovskites [15,39,40]. The lower bulk conductivity of dense BCY10 prepared by solid-state reaction (Fig. 11) is rather surprising in the absence of additional phase since the yttrium content is similar. Such a variation has been already recorded for $BaCa_{0.85}Gd_{0.15}O_{3-\delta}$ synthesized by solid-state route [40]. It is worth mentioning that a second contribution in the high frequency response of SS1600 sample could not be resolved because of the corresponding low phase angle. As no heterogeneous dopant distribution was detected within grains by EDS analysis, the origin of the recorded difference is not clarified.

As commonly observed for cerate and zirconate perovskites [21,27,32,41–43], the activation energy for the blocking effect is higher (Table 2). Values between 0.65 and 0.79 eV are in agreement with those determined for doped barium cerate [17], and further suggest that the conduction properties are identical in all samples. A higher activation energy can be understood if one assumes that oxygen ions and protons are more tightly bound together in the grain boundary region [41]. But, the values determined for bulk transport and blocking effect are lower than those for *p*-type and *n*-type conductivities [44,45]. This result supports the assumption that electronic conductivity is never more than a minor contribution in the chosen experimental conditions. One can thus infer that protons are the main charge carriers in the investigated samples. Below 350 °C for samples synthesized by sol–gel, the magnitude of the blocking effect is lower after sintering at 1600 °C (Fig. 11),

Table 2
Activation energies for BCY10 contributions and blocking thickness calculated at two temperatures.

Sample	$E(\sigma_b)$ (eV)	$E(\sigma_{bl})$ (eV)	$E(\sigma^s_{bl})$ (eV)	$E(\sigma_t)$ (eV)	δ_{bl} (150 °C) (nm)	δ_{bl} (250 °C) (nm)
SG1500	0.43	0.65	0.63	0.51	4.5	4.5
SG1550	0.44	0.77	0.79	0.54	3.3	3.6
SG1600	0.45	0.79	0.76	0.49	4.2	4.4
SS1600	0.46	0.72	0.71	0.50	4.6	4.2

as could be expected. Indeed, a high grain size (Table 1) yields a lower grain boundary density and thus a lower blocking resistance [18,46]. The absence of any significant variation of the blocking conductivity between SG1500 and SG1550 samples could be anticipated since the grain size varies only by 15%. One must keep in mind that a two-fold decrease of the blocking resistance requires a grain size increase by a factor of 1.5–2 in average [18]. The comparison of the blocking conductivities for SG1500, SG1550 and SS1600 samples emphasizes that the magnitude of the blocking effect in dense BCY10 does not depend on the elaboration route. This further suggests that the origin of the recorded blocking effects is of same nature.

The total conduction of polycrystalline ceramics is contributed by the bulk and the blocking conductivities. In the absence of any additional intergranular phase (continuous or located at triple junctions) and/or diluted impurities, the blocking effect can be ascribed to space charge layers adjacent to grain boundaries. The magnitude of the recorded effect depends mainly on the nature of the dopant and its grain boundary segregation factor, and hence represents an intrinsic property of the material [47]. The existence of an additional phase results in another contribution to the blocking effect, mostly governed by the purity of the material, which can be regarded as an extrinsic contribution to the total conduction of the ceramic [48]. To get a better insight on the electrical properties of grain boundaries, i.e. discriminate an intrinsic blocking effect from an extrinsic one, the Brick Layer Model [40] has been used. Indeed, some researchers [32,49–51] have suggested that the space charge effect may act as a blocking source for the protonic conduction in the vicinity of grain boundaries. The evidence of a space charge effect is the segregation of acceptor solutes in the grain boundaries [40,50], indicating a positive grain boundary core with adjacent negative space charge layers within protons are depleted which affects the grain boundary conductivity. For the SG1600 sample, qualitative enrichment of yttrium ions have been clearly evidenced by EDS analysis (not shown here). According to the brick Layer Model, and by assuming that the dielectric constant in grains and grain boundaries are equal [18] which is not unrealistic [52], the specific blocking conductivity σ^s_{bl} can be calculated from the blocking conductivity σ_{bl} according to:

$$\sigma^s_{bl} = \frac{1}{\sigma_{bl}} \frac{C_b}{C_{bl}} \quad (1)$$

where C_b and C_{bl} denote the geometrical capacitances of grains and grain boundaries.

The bulk capacitance C_b represents the dielectric properties of the volume of the grains and the blocking capacitance C_{bl} describes those related to the blocking of charge carriers in the vicinity of microstructure defects. Assuming plane capacitors, C_b and C_{bl} are proportional to the ratio of the electrode area to the sample thickness. Moreover, C_{bl} also depends on the ratio of the mean grain size (d_g) to the blocking thickness (δ_{bl}). The last parameter can be identified to the width of space charge layers adjacent to grain boundaries [53].

The blocking thickness can be estimated by:

$$\delta_{bl} = \frac{C_{bl}}{C_b} d_g \quad (2)$$

where d_g is the mean grain size.

If the blocking effect is controlled by impurities, one should expect an increase of the specific blocking conductivity with the grain size as the solubility of impurities would increase. Since both C_b and C_{bl} are independent of temperature (Fig. 10), the activation energy for σ^s_{bl} is similar to that for the apparent blocking conductivity (Table 2). As previously reported in the literature [28,40], the specific blocking conductivity is lower than the bulk one (Fig. 11). Grain boundaries are less conductive than grains by at least two orders of magnitude, depending on temperature. Moreover, in comparison to the blocking conductivity, the specific blocking conductivity is three orders of magnitude smaller. At 200 °C, σ^s_{bl} varies between 1 and 1.3×10^{-7} S cm^{-1} and these values are rather close to those determined in similar conditions for BCY10 [28]. At 300 °C, the specific blocking conductivity is around 2×10^{-6} S cm^{-1} which agrees with that of $BaCe_{0.9}Gd_{0.1}O_{3-\delta}$ [39]. According to the results of Fig. 11, it is apparent that the specific blocking conductivities are identical, within experimental accuracy. This has been also observed for $BaCe_{0.9}Y_{0.1}O_{3-\delta}$ synthesized by solid-state reaction and sintered at 1250 and 1500 °C respectively [28] and for $BaCe_{0.9}Gd_{0.1}O_{3-\delta}$ prepared by solid-state reaction and sintered between 1500 and 1600 °C [40]. One can thus assess that all investigated samples present the same chemical features at grain boundaries and that the electrical behaviour reported represents the inherent properties of the ceramic material. Between 150 and 350 °C, the temperature range within C_b and C_{bl} can be determined accurately, the blocking thickness is nearly constant and does not vary as function of microstructure (Table 2). For dense BCY10, δ_{bl} is of the order of 4 nm which agrees with values determined for acceptor-doped proton [40,50,54] and oxygen [55] conductors. At this stage, the results indicate that the conductivity of grain boundaries in yttrium-doped barium cerate can be analyzed by a space charge approach of a positively charged core and adjacent space charge layers depleted in positively charged defects. The electrical behaviour of grains is not affected in the presence of space charge layers. The application of $BaCeO_3$-based protonic conductors will be possible if the reported level of electrical conductivity is retained and the chemical stability, especially in gases containing CO_2, is improved. Thus, the electrical properties of yttrium-doped barium cerate-zirconate solid solutions have been investigated and will be discussed in a forthcoming paper.

4. Conclusion

By developing a versatile sol–gel method, pure BCY10 powders were synthesized after calcination at 1100 °C for 8 h in air. The final powders showed good densification since relative densities higher than 95% of the theoretical one and homogeneous microstructures were achieved after sintering above 1400 °C. The conductivities of selected sol–gel samples were characterized by impedance spectroscopy versus temperature in wet argon and compared to those of BCY10 elaborated by solid-state reaction. The electrical properties are in overall agreement with the literature and reflect a protonic conductivity. At 600 °C, the total conductivity of sol–gel samples (grain size: 5–9 μm) is the same and comparable to the state-of-art cerate materials. At high temperatures, the electrical properties of grains rule the total conductivity and the blocking effect due to grain boundaries becomes increasingly predominant on lowering temperature. The electrical contribution of grain boundaries can be related to the existence of space charge layers. The specific blocking conductivity is the same, regardless of both grain size and elaboration route, indicating that the different behaviour is determined by the grain size.

References

[1] H. Iwahara, T. Esaka, H. Uchida, N. Maeda, Solid State Ionics 3–4 (1981) 359–363.
[2] H. Uchida, N. Maeda, H. Iwahara, Solid State Ionics 11 (1983) 117–124.
[3] H. Iwahara, Solid State Ionics 77 (1995) 289–298.
[4] N. Fukatsu, N. Kurita, T. Kajima, K. Koide, T. Ohashi, J. Alloys Compd. 231 (1995) 706–712.
[5] N. Fukatsu, N. Kurita, K. Koide, T. Ohashi, Solid State Ionics 113–115 (1998) 219–227.
[6] T. Norby, Solid State Ionics 125 (1999) 1–11.
[7] T. Schober, Solid State Ionics 162–163 (2003) 277–281.
[8] H. Iwahara, Y. Asakura, K. Katahira, M. Tanaka, Solid State Ionics 168 (2004) 299–310.

[9] T. Schober, F. Krug, W. Shilling, Solid State Ionics 97 (1997) 369–373.
[10] N. Bonanos, K.S. Knight, B. Ellis, Solid State Ionics 79 (1995) 161–170.
[11] D.A. Stevenson, N. Jiang, R.M. Buchanan, F.E.G. Nenn, Solid State Ionics 62 (1993) 279–285.
[12] R.C.T. Slade, N. Singh, Solid State Ionics 61 (1993) 111–114.
[13] F.L. Chen, O.T. Sorensen, G.Y. Meng, D.K. Peng, J. Eur. Ceram. Soc. 18 (1998) 1389–1395.
[14] K. Katahira, Y. Kohchi, T. Shimura, H. Iwahara, Solid State Ionics 138 (2000) 91–98.
[15] W. Grover Coors, D.W. Readey, J. Am. Ceram. Soc. 85 (2002) 2637–2640.
[16] M.H. Zheng, B. Zhu, Solid State Ionics 80 (1995) 59–65.
[17] S.D. Flint, R.C.T. Slade, Solid State Ionics 77 (1995) 215–221.
[18] S.M. Haïle, G. STaneff, K.H. Ryu, J. Mater. Sci. 36 (2001) 1149–1160.
[19] E. Fabbri, A. D'Epifanio, E. Di Bartolomeo, S. Licoccia, E. Traversa, Solid State Ionics 179 (2008) 558–564.
[20] Z. Zhong, Solid State Ionics 178 (2007) 213–220.
[21] M. Amsif, D. Marrero-Lopez, A. Magraso, J. Pena-Martinez, J.C. Ruiz-Morales, P. Nunez, J. Eur. Ceram. Soc. 29 (2009) 131–138.
[22] V. Agarwal, M. Liu, J. Mater. Sci. 32 (1997) 619–625.
[23] S. Liu, X. Tan, K. Li, R. Hughes, Ceram. Int. 28 (2002) 327–335.
[24] F. Chen, O.T. Sorensen, G. Meng, D. Peng, Solid State Ionics 100 (1997) 63–72.
[25] A.P. Almeida de Oliveira, J. Hafsaoui, J.-F. Hochepied, M.-H. Berger, A. Thorel, J. Eur. Ceram. Soc. 27 (2007) 3597–3600.
[26] M. Kleitz, L. Dessemond, M.C. Steil, Solid State Ionics 75 (1995) 107–115.
[27] G. Chiodelli, L. Malavasi, C. Realdi, S. Barison, M. Battagliarin, L. Doubova, M. Fabrizio, C. Mortalo, R. Gerbasi, J. Alloys Compd. 170 (2009) 477–485.
[28] A. Bassano, V. Buscaglia, M. Viviani, M. Bassoli, M.T. Buscaglia, M. Sennour, A. Thorel, P. Nanni, Solid State Ionics 180 (2009) 168–174.
[29] J. Tong, D. Clark, L. Bernau, A. Subramaniyan, R. O'Hayre, Solid State Ionics 181 (2010) 1486–1498.
[30] N. Bonanos, B. Ellis, K.S. Knight, M.N. Mahood, Solid State Ionics 35 (1989) 179–188.
[31] F.M.M. Snijkers, D. Buekenhoudt, J. Cooymans, J.J. Luyten, Scripta Mater. 50 (2004) 655–659.
[32] S.B.C. Duval, P. Holtappels, U.F. Vogt, E. Pomjakushina, K. Conder, U. Stimming, T. Graule, Solid State Ionics 178 (2007) 1437–1441.
[33] S. Imashuku, T. Uda, Y. Nose, Y. Awakura, J. Alloys Compd. 490 (2010) 665–675.
[34] I. Ahmed, S.-G. Erikson, E. Ahlberg, C.S. Knee, Solid State Ionics 179 (2008) 1155–1160.
[35] Y. Guo, B. Liu, Q. yang, C. Chen, W. Wang, G. Ma, Electrochem. Commun. 11 (2008) 153–156.
[36] A.S. Nowick, Y. Du, Solid State Ionics 77 (1995) 137–146.
[37] N. Kurita, N. Fukatsu, K. Ito, T. Ohashi, J. Electrochem. Soc. 142 (1995) 1552–1559.
[38] A. Grimaud, J.M. Bassat, F. Mauvy, P. Simon, A. Canizares, B. Rousseau, M. Marrony, J.C. Grenier, Solid State Ionics 191 (2011) 24–31.
[39] K.H. Ryu, J.M. Haile, Solid State Ionics 125 (1999) 355–367.
[40] S.M. Haile, D.L. West, J. Campbell, J. Mater. Res. 13 (1998) 1576–1595.
[41] S.B.C. Duval, P. Holtappels, U. Stimming, T. Graule, Solid State Ionics 179 (2008) 1112–1115.
[42] F. Iguchi, T. Yamada, N. Sata, T. Tsurui, H. Yugumi, Solid State Ionics 177 (2006) 2381–2384.
[43] P. Pasierb, M. Wierzbicka, S. Komornicki, M. Rekas, J. Power Sources 173 (2007) 681–687.
[44] I. Kosacki, H.L. Tuller, Solid State Ionics 80 (1995) 223–229.
[45] A.R. Potter, R.T. Baker, Solid State Ionics 177 (2006) 1917–1924.
[46] R.B. Cervera, Y. Oyama, S. Miyoshi, K. Kobayashi, T. Yagi, S. Yamaguchi, Solid State Ionics 179 (2008) 236–242.
[47] X. Guo, W. Sigle, J. Maier, J. Am. Ceram. Soc. 86 (2003) 77–87.
[48] M. Aoki, Y.M. Chiang, I. Kosacki, L.J. Lee, H. Tuller, Y. Liu, J. Am. Ceram. Soc. 79 (1996) 1169–1180.
[49] F. Iguchi, N. Sata, T. Tsurui, H. Yugami, Solid State Ionics 178 (2007) 691–695.
[50] C. Kjolseth, H. Fjeld, O. Prytz, P.I. Dahl, C. Estournes, R. Haugsrud, T. Norby, Solid State Ionics 181 (2010) 268–275.
[51] H. Fjeld, D.M. Kepaptsoglou, R. Haugsrud, T. Norby, Solid State Ionics 181 (2010) 104–109.
[52] M. Vollmann, R. Waser, J. Am. Ceram. Soc. 77 (1994) 235–243.
[53] X. Guo, J. Maier, J. Electrochem. Soc. 148 (2001) E121–E126.
[54] H.G. Bohn, T. Schober, T. Mono, W. Scilling, Solid State Ionics 177 (1999) 219–228.
[55] X. Guo, R. Waser, Prog. Mater. Sci. 51 (2006) 151–210.